J|A|C|S
ARTICLES
Published on Web 02/16/2007

Binding Induced Folding in p53−MDM2 Complex

Hai-Feng Chen and Ray Luo*

Contribution from the Department of Molecular Biology and Biochemistry, University of California, Irvine, California 92697-3900

Received November 3, 2006; E-mail: rluo@uci.edu

Abstract: The MDM2 N-terminal domain can bind to the transactivation domain of p53 and downregulate its ability to activate transcription. It was found that binding with p53 stabilizes the MDM2 N-terminal domain. Thus the coupling between binding and folding is essential in the normal functional interactions between p53 and MDM2. We have performed explicit-solvent molecular dynamics simulations (MD) for both bound $MDM2^N$ and apo-MDM2 to study the interdependence of binding and folding in the p53−MDM2 complex. Kinetic analysis of high-temperature MD simulations shows that both bound $MDM2^N$ and apo-MDM2 unfold via a two-state process. Both kinetics and free energy landscape analyses indicate that bound MDM2 unfolds in the order of p53 unbinding, tertiary unfolding, and finally secondary structure unfolding. Our data show that the unfolding pathways are different between bound $MDM2^N$ and apo-MDM2: the unfolding order of unstable helices and tertiary contacts is reversed. Transition state analysis shows that the transition state of bound MDM2 is more nativelike and more heterogeneous than that of apo-MDM2. The predicted Φ-values suggest that the stable helices are more nativelike than other regions in both bound $MDM2^N$ and apo-MDM2. Within the stable helices, helix II in bound MDM2 is more nativelike than that in apo-MDM2. However, helix I and IV in bound MDM2 are less nativelike than those in apo-MDM2.

Introduction

The human version of mouse double minute protein 2 (MDM2) has 491 residues. Its best known biological role is to negatively regulate the tumor-suppressor activity of p53 when its N-terminal domain ($MDM2^N$) binds to the transactivation domain of p53.[1−4] Because of its importance in cancer development, the $MDM2^N$−p53 complex is a target for anticancer drug design[5,6] to restore normal p53 function in tumor cells and to induce growth suppression and apoptosis.[7,8]

The crystal structure for the $MDM2^N$−p53 complex was reported in 1996 (pdb code: 1YCR).[3] The complex has five α-helices and two strands of antiparallel β-sheets. $MDM2^N$ consists of helix I from Pro32 to Val41, helix II from Met50 to Lys64, helix III from Leu81 to Phe86, helix IV from His96 to Asn106, strand I from Ile74 to Tyr76, and strand II from Ser90 to Ser92. p53 consists of helix V from Phe18 to Leu25. Two longer helices (helix II and IV) and two shorter helices (helix I and III) form a deep hydrophobic cleft for p53 binding in $MDM2^N$ (see Figure 1).

NMR experiments indicate that $MDM2^N$ is unstable.[9] There is evidence of partial unfolding and multiple conformations.[9]

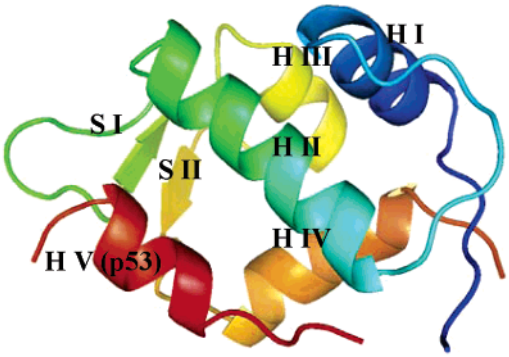

Figure 1. Ribbon representation of the X-ray structure of p53-$MDM2^N$ (pdb code: 1YCR). Blue represents helix I, green represents helix II, yellow represents helix III, orange represents helix IV, and red represents helix V.

$MDM2^N$ becomes several-fold more stable in the presence of peptide or small-molecule ligands.[9] When $MDM2^N$ interacts with p53, chemical shifts are changed not only in the binding pocket of the protein but also over other parts of the protein, suggesting global conformational change in $MDM2^N$.[10] These experimental observations raise a series of interesting questions. (1) How does the folded state of $MDM2^N$ change upon p53 binding? (2) How does p53 binding influence the folding pathway of $MDM2^N$? (3) How does p53 binding influence the unfolded state of $MDM2^N$? To answer these questions, we utilize

(1) Juven-Gershon, T.; Oren, M. *Mol. Med.* **1999**, *5*, 71−83.
(2) Oliner, J. D.; Kinzler, K. W.; Meltzer, P. S.; George, D. L.; Vogelstein, B. *Nature* **1992**, *358*, 80−83.
(3) Kussie, P. H.; Gorina, S.; Marechal, V.; Elenbaas, B.; Moreau, J.; Levine, A. J.; Pavletich, N. P. *Science* **1996**, *274*, 948−953.
(4) Momand, J.; Jung, D.; Wilczynski, S.; Niland, J. *Nucleic Acids Res.* **1998**, *26*, 3453−3459.
(5) Vassilev, L. T.; Vu, B. T.; Graves, B.; Carvajal, D.; Podlaski, F.; Filipovic, Z.; Kong, N.; Kammlott, U.; Lukacs, C.; Klein, C.; Fotouhi, N.; Liu, E. A. *Science* **2004**, *303*, 844−848.
(6) Zhong, H.; Carlson, H. A. *Proteins* **2005**, *58*, 222−234.
(7) Bullock, A. N.; Fersht, A. R. *Nat. Rev. Cancer* **2001**, *1*, 68−76.
(8) Zhang, R.; Mayhood, T.; Lipari, P.; Wang, Y.; Durkin, J.; Syto, R.; Gesell, J.; McNemar, C.; Windsor, W. *Anal. Biochem.* **2004**, *331*, 138−146.
(9) Uhrinova, S.; Uhrin, D.; Powers, H.; Watt, K.; Zheleva, D.; Fischer, P.; McInnes, C.; Barlow, P. N. *J. Mol. Biol.* **2005**, *350*, 587−598.
(10) Schon, O.; Friedler, A.; Bycroft, M.; Freund, S. M.; Fersht, A. R. *J. Mol. Biol.* **2002**, *323*, 491−501.

10.1021/ja0678774 CCC: $37.00

molecular dynamics (MD) simulations in explicit solvent to analyze the coupling between binding and folding[11,12] in the MDM2^N−p53 complex.

However the folding time scales of most single-domain proteins, 10−1000 μs as recent ultrafast spectroscopy experiments have shown,[13−15] are much longer than those of MD simulations. The longest single simulation trajectory performed so far is about 1 μs on the ab initio folding of a villin headpiece, a small protein domain of only 36 residues.[16] In order to study protein folding within reasonable time, simulations of protein unfolding have been widely used.[17−25] This is because the rate of unfolding increases at high temperatures, for example, at as high as 498 K, so that most single-domain proteins unfold in the nanosecond time scale.[26] Although high-temperature simulations could favor uncharacteristic and/or "fast-track" pathways,[27] they have been found to yield room-temperature folding pathways consistent with experimental measurements.[26] Indeed, a number of interesting observations have emerged from MD unfolding simulations of many small globular proteins.[17−25] Ideally, room-temperature folding simulations would be used to study the coupling between binding and folding in the MDM2^N−p53 complex. However, it is impossible to accumulate long enough trajectories to draw any meaningful conclusions. Therefore, unfolding simulations at high temperature have been used in the current study.

In the following, we will discuss the unfolding kinetics, unfolding landscapes, transition states, unfolded states, and folded states for both bound MDM2^N and apo-MDM2^N to understand the influence of binding in the folding of MDM2^N.

Results and Discussion

Unfolding Kinetics. Native tertiary contacts (Qf) and native binding contacts (Qb) are used to monitor unfolding and unbinding kinetics. Time evolutions of Qb and Qf for bound MDM2^N are shown in Figure 2. Overall, the tertiary unfolding and unbinding kinetics can be represented well by single-exponential functions, indicating that they are first-order kinetics in the NVT ensemble at 498 K but with the room-temperature water density. The fitted kinetics data are shown in Table 1. Our kinetics analysis shows that the unbinding half time is 0.21 ns, and the unfolding half time is 1.27 ns, indicating that unbinding is much faster than tertiary unfolding. The time evolution of Qf for apo-MDM2^N is also shown in Figure 2. It is found that tertiary unfolding of apo-MDM2^N also obeys first-order kinetics, with a half time of 1.36 ns, which is very similar to that of bound MDM2^N.

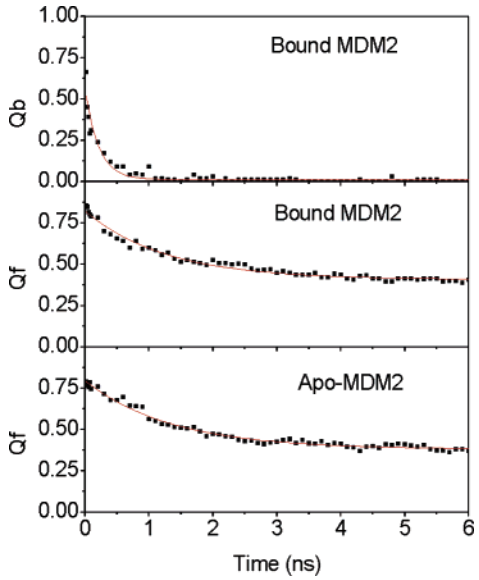

Figure 2. Kinetics fitting of Qb and Qf for bound MDM2^N and apo-MDM2^N.

Table 1. Unfolding Kinetics Constants[a]

		τ (ns)	A	B	R^2
bound MDM2	Qb	0.21	0.56	0.0011	0.94
	Qf	1.27	0.41	0.41	0.98
	helix I, II, and IV	3.58	0.36	0.53	0.86
	helix III and V	1.70	0.29	0.29	0.67
apo-MDM2	Qf	1.36	0.42	0.38	0.98
	helix I, II, and IV	2.36	0.51	0.49	0.90
	helix III	0.34	0.56	0.25	0.86

[a] All curves are fitted by $A \exp(-t/\tau) + B$.

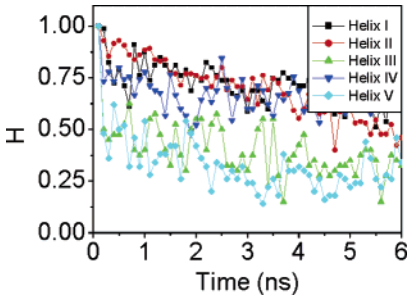

Figure 3. Unfolding of five helices in bound MDM2^N. H is fractional native helical content.

Unfolding kinetics of all five helices is also analyzed and presented in Figure 3. It was found that the five helices can be grouped into two categories: stable helices (I, II, and IV) and unstable helices (III and V). Time evolution curves for both stable and unstable helices in both bound MDM2^N and apo-MDM2^N, respectively, are shown in Figure 4. Our analysis shows that helix unfolding also obeys first-order kinetics under the high-temperature simulation condition. The unfolding half time is 1.70 ns for unstable helices and 3.58 ns for stable helices, respectively, in bound MDM2^N. The unfolding half time is 2.36 ns for stable helices and about 0.39 ns for unstable helices (III only), respectively, in apo-MDM2^N. Not surprisingly, helical

(11) Henkels, C. H.; Kurz, J. C.; Fierke, C. A.; Oas, T. G. *Biochemistry* **2001**, *40*, 2777−2789.
(12) Henkels, C. H.; Oas, T. G. *J. Am. Chem. Soc.* **2006**, *128*, 7772−7781.
(13) Williams, S.; Causgrove, T. P.; Gilmanshin, R.; Fang, K. S.; Callender, R. H.; Woodruff, W. H.; Dyer, R. B. *Biochemistry* **1996**, *35*, 691−697.
(14) Munoz, V.; Thompson, P. A.; Hofrichter, J.; Eaton, W. A. *Nature* **1997**, *390*, 196−199.
(15) Lapidus, L. J.; Eaton, W. A.; Hofrichter, J. *Proc. Natl. Acad. Sci. U.S.A.* **2000**, *97*, 7220−7225.
(16) Duan, Y.; Kollman, P. A. *Science* **1998**, *282*, 740−744.
(17) Caflisch, A.; Karplus, M. *Proc. Natl. Acad. Sci. U.S.A.* **1994**, *91*, 1746−1750.
(18) Caflisch, A.; Karplus, M. *J. Mol. Biol.* **1995**, *252*, 672−708.
(19) Daggett, V.; Li, A. J.; Itzhaki, L. S.; Otzen, D. E.; Fersht, A. R. *J. Mol. Biol.* **1996**, *257*, 430−440.
(20) Ladurner, A. G.; Itzhaki, L. S.; Daggett, V.; Fersht, A. R. *Proc. Natl. Acad. Sci. U.S.A.* **1998**, *95*, 8473−8478.
(21) Tsai, J.; Levitt, M.; Baker, D. *J. Mol. Biol.* **1999**, *291*, 215−225.
(22) Mayor, U.; Johnson, C. M.; Daggett, V.; Fersht, A. R. *Proc. Natl. Acad. Sci. U.S.A.* **2000**, *97*, 13518−13522.
(23) Gsponer, J.; Caflisch, A. *J. Mol. Biol.* **2001**, *309*, 285−298.
(24) Mayor, U.; Guydosh, N. R.; Johnson, C. M.; Grossmann, J. G.; Sato, S.; Jas, G. S.; Freund, S. M. V.; Alonso, D. O. V.; Daggett, V.; Fersht, A. R. *Nature* **2003**, *421*, 863−867.
(25) Scott, K. A.; Randles, L. G.; Moran, S. J.; Daggett, V.; Clarke, J. *J. Mol. Biol.* **2006**, *359*, 159−173.
(26) Fersht, A. R.; Daggett, V. *Cell* **2002**, *108*, 573−582.
(27) Dinner, A. R.; Karplus, M. *J. Mol. Biol.* **1999**, *292*, 403−419.

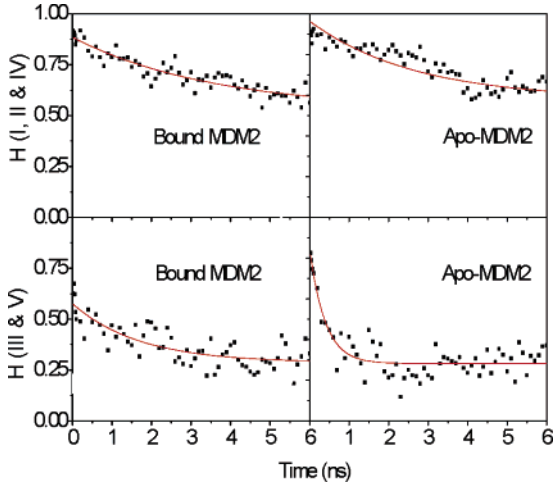

Figure 4. Kinetics fitting for stable helices (I, II, and IV) and unstable helices (III and V) or helix III for bound MDM2^N and apo-MDM2^N, respectively.

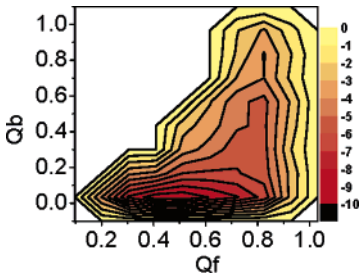

Figure 5. Unfolding landscapes with respect to Qb and Qf for bound MDM2^N.

unfolding is slower than tertiary unfolding and unbinding. This is consistent with other unfolding simulations of helical proteins, for example, chymotrypsin inhibitor 2.[28] Note also that the helical unfolding half times of the bound MDM2^N are longer than those of apo-MDM2^N, suggesting that binding to p53 stabilizes the helices in MDM2^N.[29] Finally, since the two short beta strands are too weak, they are not monitored during unfolding.

Unfolding Landscapes. To further understand the coupling between unfolding and unbinding, the unfolding landscape of bound MDM2^N was analyzed with the progress variables Qf and Qb, as shown in Figure 5. The unfolding landscape shows that unbinding proceeds first while tertiary contacts are held stable. This is followed by tertiary unfolding. This is in agreement with the unfolding kinetics analysis for the bound MDM2^N. Note also that even if the time scale of unbinding is much shorter than that of tertiary unfolding, there is no rapid transition between binding and unbinding during tertiary unfolding. This suggests the formation of binding interface depends on formation of overall tertiary contacts, different from the coupling between secondary unfolding and tertiary unfolding to be shown below.

The coupling between secondary and tertiary unfolding is studied for both bound MDM2^N and apo-MDM2^N and is shown in Figure 6. Since the two short beta strands are too weak, only helical structures were monitored during unfolding. The coupling between stable helices and tertiary contacts in unfolding is

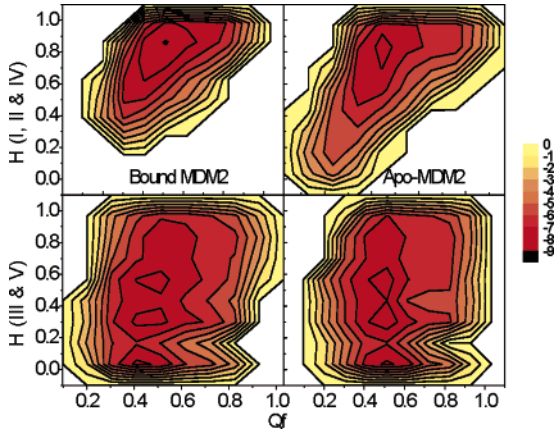

Figure 6. Unfolding landscapes with H and Qf for bound MDM2^N and apo-MDM2^N, respectively.

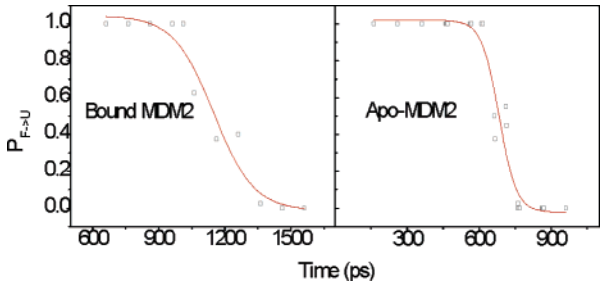

Figure 7. A representative transition probability P calculated at 498 K for the F ⇔ U transition for snapshot in the transition region for one of trajectories for bound MDM2^N and apo-MDM2^N, respectively. The red line is the fit to $P = 1/\{1 + \exp[(\tau - \tau_{TS})/\tau_{trans}]\}$. See text for more information on the fit.

shown in Figure 6. It is found that Qf decreases first while stable helical content does not change. This is followed by a simultaneous decrease of tertiary contacts and stable helical content. This suggests that the tertiary unfolding is followed by secondary and tertiary unfolding. This is also consistent with the above unfolding kinetics analysis. The coupling between unstable helical content and tertiary contacts is also monitored as shown in Figure 6. We found that unstable helices (III and V) are in rapid transition between folding and unfolding during tertiary unfolding due to their fast folding/unfolding rates. This is different from binding, even if its time scale is similar to that of the unstable helix in apo-MDM2^N.

Transition State. Our kinetics analysis shows that tertiary unfolding of both bound MDM2^N and apo-MDM2^N obey first-order kinetics. This suggests that bound MDM2^N and apo-MDM2^N unfold via a two-state process. Therefore, there is a transition state that corresponds to the free energy maximum along each of their unfolding pathways. The structures at the free energy maxima comprise the transition state ensemble (TSE). TSE structures can either fold or unfold, and the transition probability (P) will be 50%. We have scanned MD snapshots for TSE structures in all 10 unfolding trajectories for each of the bound MDM2^N and apo-MDM2^N, respectively.[30] Transition probabilities versus candidate snapshot are shown in Figure 7. The transition probability curves are further fitted by the Boltzmann equation, $P = 1/(1 + \exp((t - \tau_{TS})/\tau_{trans}))$, where τ_{TS} is the time when $P = 50\%$ and τ_{trans} sets the period

(28) Day, R.; Daggett, V. *Protein Sci.* **2005**, *14*, 1242−1252.
(29) Petsko, G. A.; Ringe, D. *Protein Structure and Function*; New Science Press: London, 2003.
(30) Pande, V. S.; Rokhsar, D. S. *Proc. Natl. Acad. Sci. U.S.A.* **1999**, *96*, 9062−9067.

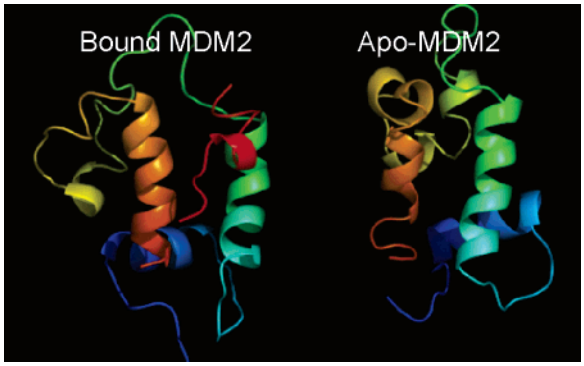

Figure 8. Average TSE structures for bound MDM2^N and apo-MDM2^N, respectively.

when P is between 0.4 and 0.6.[30−32] Our analysis yields 382 snapshots for bound MDM2^N TSE and 271 snapshots for apo-MDM2^N TSE, respectively.

Figure 8 illustrates the average structures for all TSE snapshots for bound MDM2^N and apo-MDM2^N, respectively. Apparently from Figure 8, the TSE of apo-MDM2^N is less-structured than that of bound MDM2^N. Indeed, there are 50% native hydrophobic contacts, 70.5% stable helical content, and 23.9% unstable native helical content for the apo-MDM2^N TSE, while there are 57% native hydrophobic contacts, 84.6% stable native helical content, and 37.0% unstable native helical content for bound MDM2^N. Overall, it can be concluded that the TSE of bound MDM2^N is more nativelike than that of apo-MDM2^N. This indicates that the folding activation free energy for bound MDM2^N is probably smaller than that for apo-MDM2^N, leading to a relatively faster folding rate for bound MDM2^N. Combining with the above analysis that the unfolding rates for bound MDM2^N and apo-MDM2^N are virtually the same, this leads to the conclusion that bound MDM2^N is more stable than apo-MDM2^N, based on the following relationship for two-state folding systems,[33] $K=k_f/k_u$, where K is folding equilibrium constant, k_f and k_u are folding and unfolding rates, respectively. This conclusion on the relative stability between bound MDM2^N and apo-MDM2^N is consistent with the previous experimental observation.[9]

Figure 9 illustrates structural variations of TSE structures for bound MDM2^N and apo-MDM2^N, respectively. The Cα fluctuation of bound MDM2^N is larger than that of apo-MDM2^N, suggesting that bound MDM2^N is more heterogeneous than that of apo-MDM2^N at the transition state. Thus TSE for bound MDM2^N is more nativelike and more heterogeneous than that for apo-MDM2^N. However, the Φ/Ψ fluctuation of bound MDM2^N is similar to that of apo-MDM2^N: there are three stable helices with low fluctuation in both states.

Finally, all TSE snapshots were used to predict Φ-values of bound MDM2^N and apo-MDM2^N as shown in Figure 10. The sequence distribution of Φ-values suggests that the three stable helices identified in the above structural variation analysis (Figure 9) are more nativelike than other regions for both bound MDM2^N and apo-MDM2^N. Within the three stable helices, the Φ-values of helix II for bound MDM2^N are larger than those

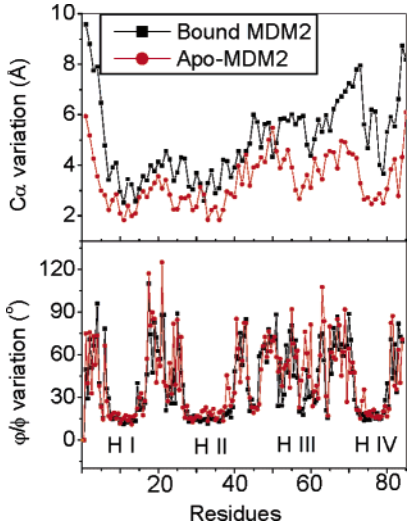

Figure 9. Cα and Φ/Ψ variations at TSE for bound MDM2^N and apo-MDM2^N, respectively.

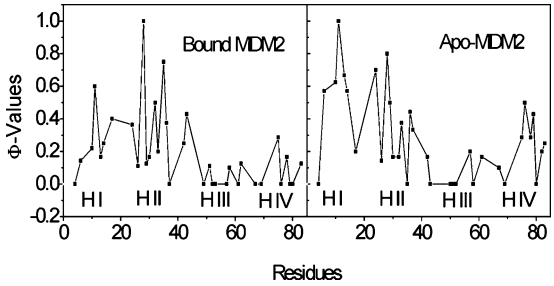

Figure 10. Predicted Φ-values for bound MDM2^N and apo-MDM2^N, respectively.

of apo-MDM2^N. However the Φ-values of helix I and IV for bound MDM2^N are smaller than those of apo-MDM2^N.

Unfolded State. All unfolding simulations eventually reach the unfolded equilibrium state under the high-temperature unfolding condition. For the unfolded state of bound MDM2^N, there are 41.2% native hydrophobic contacts, 67.8% stable helical content, and 36.5% unstable helical content remaining. Worth noting is the fact that the hydrophobic intrahelix contacts on the unstable helix III all disappear. There is still a well-defined hydrophobic cluster among the three stable helices. This is very different from that of the apo-MDM2^N, for which the hydrophobic contacts are divided into two clusters. One is located between helix I and II, and the other is on helix IV. There are 35.3% native hydrophobic contacts, 59.6% stable helical content, and 41.5% unstable helical content remaining.

Conformational fluctuation was also analyzed using structural variation from the average structures for the unfolded state (Figure 11). The Cα fluctuation of bound MDM2^N is larger than that of apo-MDM2^N, indicating that bound molecules are more heterogeneous. This is similar to the transition state structures analyzed above. Also similar to the transition state, there is little difference in the Φ/Ψ fluctuation between bound MDM2^N and apo-MDM2^N.

Folded State. As a reference for the above unfolding simulations and to further compare with experiment by structures and dynamics, 10 trajectories of 10.0 ns each were simulated at 298 K to analyze the folded state of apo-MDM2^N, apo-p53, and their complex, respectively. Here, the structural influence

(31) Gsponer, J.; Caflisch, A. *Proc. Natl. Acad. Sci. U.S.A.* **2002**, *99*, 6719−6724.
(32) Chong, L. T.; Snow, C. D.; Rhee, Y. M.; Pande, V. S. *J. Mol. Biol.* **2005**, *345*, 869−878.
(33) Nolting, B. *Protein Folding Kinetics, Biophysical Methods*; Springer: Berlin, 1999.

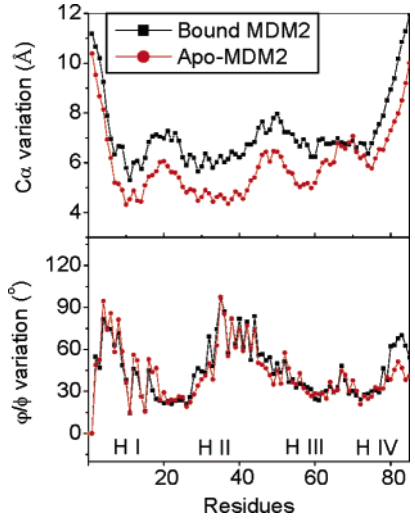

Figure 11. Cα and Φ/Ψ variations at the unfolded state for bound MDM2^N and apo-MDM2^N, respectively.

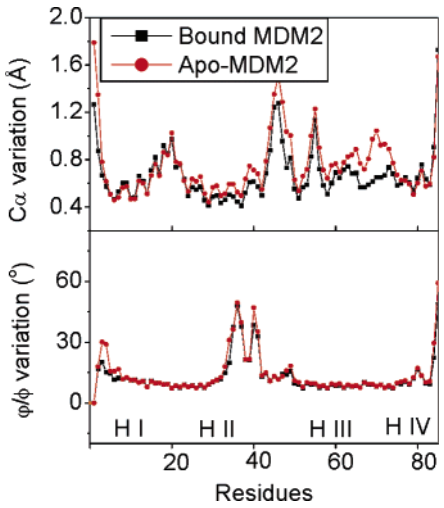

Figure 12. Cα and Φ/Ψ variations at the folded state for bound MDM2^N and apo-MDM2^N, respectively.

of p53 binding on the folded MDM2^N is first analyzed. It has been observed in experiment that MDM2^N must undergo an expansion upon p53 binding, achieved through a rearrangement and outward expansion of the helices surrounding the binding cleft.[9] To make the statement quantitative for easy comparison, the distance between the centers of helix II and IV at the cleft opening in the experimental structures is measured and is found to increase by 0.5 Å upon p53 binding.[9] In simulation, the average distance between the centers of the same helices increases by about 0.7 Å upon p53 binding, in qualitative agreement with experiment. In addition, the distance between the centers of helix I and III at the cleft bottom in the experimental structures increases by 0.8 Å upon p53 binding. In simulation, the average distance between the centers of the same helices increases by 0.5 Å, also in qualitative agreement with experiment.[9]

To study the influence of p53 binding on the dynamics of the folded MDM2^N, Cα and Φ/Ψ variations for bound MDM2^N and apo-MDM2^N are analyzed and shown in Figure 12. The Cα variation of bound MDM2^N is smaller than that of apo-MDM2^N, especially in the loop connecting helix II and III and the loop connecting helix III and IV at the p53 binding site. This suggests that bound MDM2^N becomes less flexible and more stable upon p53 binding, consistent with experiment.[9] The Φ/Ψ variation of bound MDM2^N is similar to that of apo-MDM2^N, suggesting that secondary structure stabilities have no significant change upon p53 binding. Indeed, helices I, III, and IV are already very stable in apo-MDM2^N. Helix II undergoes large fluctuating motions in both bound MDM2^N and apo-MDM2^N as observed in experiment.[9] Main-chain-based clustering analysis is also performed to investigate conformational fluctuation and stability in bound MDM2^N and apo-MDM2^N. There are 9 main-chain clusters for bound MDM2^N and 16 main-chain clusters for apo-MDM2^N. This is also consistent with the experimental observation that bound MDM2^N is more rigid and less disordered.[9]

To understand the causes for binding induced change in the folded state, interactions between p53 and MDM2^N were analyzed. All possible hydrophobic and hydrogen-bonding contacts in the crystal structure were identified with Ligplot,[34] as shown in Figure 13. The populations of eight hydrophobic contacts in simulation are shown in Figure 14A. Five stable hydrophobic interactions can be found: Phe19/Ile61, Trp23/Ile61, Leu22/Val93, Phe19/Met62, and Phe19/Val75, with populations higher than 60%. The other three hydrophobic interactions are rather unstable. The structural analysis by Kussie et al. shows that Phe19 and Trp23 are in van der Waals contact with Ile61.[3] Besides hydrophobic interactions, four possible hydrogen bonds were also identified with Ligplot.[34] Figure 14B shows their populations in simulation. However, only one stable hydrogen bond (Trp23/Leu54) exists, with a population higher than 60%. There is also one marginally stable hydrogen bond (Phe19/Gln72) with a population around 30%. The other two hydrogen bonds are very weak. This is consistent with the structural analysis by Kussie et al.[3] Comparing hydrophobic and hydrogen-bonding interactions, hydrophobic interactions play a key role in stabilizing the protein−protein interface as in most protein−protein interactions.[29] In summary, p53 binding introduced more hydrophobic contacts at the interface and within MDM2^N which are responsible for the higher stability in MDM2^N.

Unfolding Pathways and Likely Folding Pathways. Based on the unfolding kinetics, landscape analysis, and transition state analysis, unfolding pathways for bound MDM2^N can now be constructed as shown in Figure 15. (1) At the unbinding half time, there are 23 out of 34 (folded state) native hydrophobic contacts within MDM2^N. Most lost hydrophobic contacts are with Helix I. The native hydrophobic contacts between p53 and MDM2^N also start to disappear: only 1 out of 5 exists. There are 90.1% stable helical content and 57.2% unstable helical content remaining. The two short beta strands have disappeared. (2) At the half time of tertiary unfolding, there are 20 native hydrophobic contacts within MDM2^N. The hydrophobic core is located mostly among the stable helices. All native hydrophobic contacts between p53 (one of the unstable helix) and MDM2^N have disappeared. There are 83.2% stable helical content and 48.4% unstable helical content remaining. (3) At the half time of unstable helix (III and V) unfolding, there are 19 native hydrophobic contacts, and they are located among the stable helices only. There are 82.4% native stable helical

(34) Wallace, A. C.; Laskowski, R. A.; Thornton, J. M. *Protein Eng.* **1995**, *8*, 127−134.

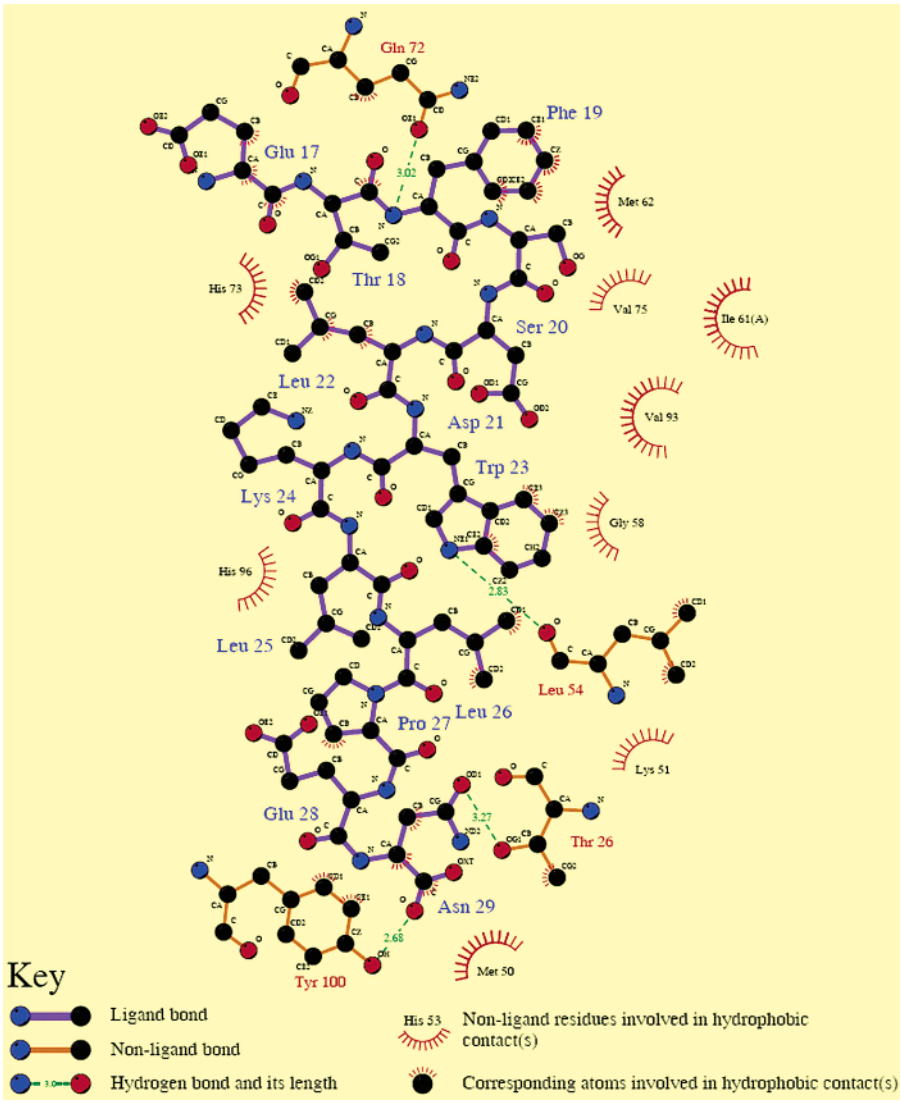

Figure 13. Two-dimensional representation for the interactions between p53 and MDM2^N.

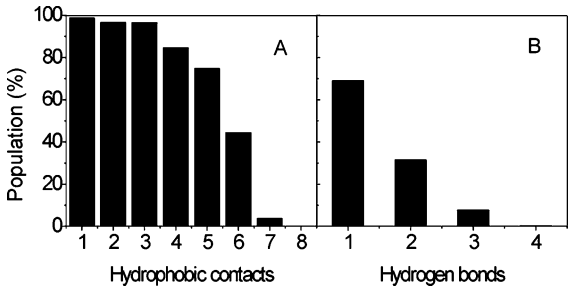

Figure 14. Interactions between p53 and MDM2^N. (A) Hydrophobic contacts. 1 is for Phe19/Ile61; 2, for Trp23/Ile61; 3, for Leu22/Val93; 4, for Phe19/Met62; 5, for Phe19/Val75; 6, for Pro27/Tyr100; 7, for Trp23/Met62; and 8, for Pro27/Met50. (B) Hydrogen bonds. 1 is for NE1(Trp23)/O(Leu54); 2, for N(Phe19)/OE1(Gln72); 3, for O(Asn29)/OH(Tyr100); and 4, for OD1(Asn29)/OG1(Thr26).

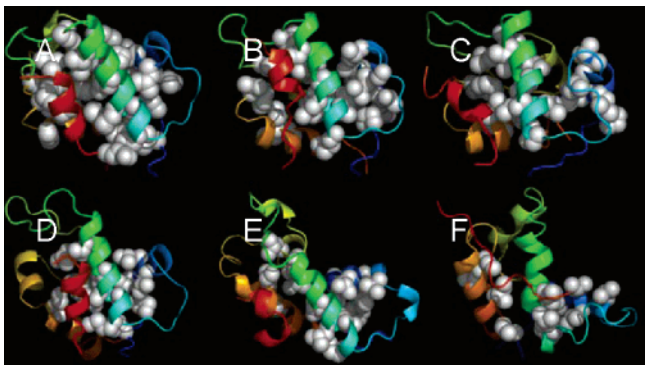

Figure 15. Unfolding pathway of bound MDM2^N. (A) <0 ns (F), (B) 0.21 ns (τ_{Qb}), (C) 1.27 ns (τ_{Qf}), (D) 1.70 ns ($\tau_{H3/5}$), (E) 3.58 ns ($\tau_{H1/2/4}$), and (F) >6 ns (U).

content and 47.7% unstable helical content remaining. (4) At the half time of stable helix (I, II, and IV) unfolding, there are 16 native hydrophobic contacts among the three stable helices. The hydrophobic core is broken into two clusters, one centered on helix I and the other between helix II and helix IV. There are 78.3% native stable helical content and 36.5% native unstable helical content remaining. The average time for visiting the transition state is between the half times of unstable helical unfolding and stable helical unfolding.

Similarly, the unfolding pathway of apo-MDM2^N is constructed and shown in Figure 16. (1) At the half time of unstable helix (III) unfolding, there are 21 out of 32 (folded state) native hydrophobic contacts. Most lost hydrophobic contacts are with helix II. There are 85.9% stable helical content and 42.4%

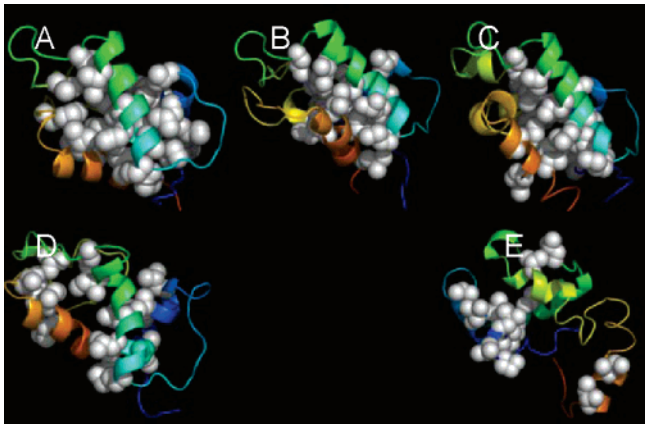

Figure 16. Unfolding pathway of apo-MDM2^N. (A) <0 ns (F), (B) 0.39 ns (τ_{H3}), (C) 1.36 ns (τ_{Qf}), (D) 2.36 ns ($\tau_{H1/2/4}$), and (E) >6 ns (U).

unstable helical content remaining. (2) At the half time of tertiary unfolding, there are 16 native hydrophobic contacts. The hydrophobic core is located mostly among the stable helices. There are 82.0% stable helical content and 41.6% unstable helical content remaining. (3) At the half time of stable helix (I, II and IV) unfolding, there are 17 native hydrophobic contacts. The hydrophobic core among the stable helices has significantly unpacked into multiple clusters. There are 82.3% stable helical content and 21.6% unstable helical content remaining. The average time for visiting the transition state is between the half times of tertiary unfolding and stable helical unfolding.

If we assume that folding is the reverse of unfolding, the proposed folding/binding pathway of bound MDM2^N is stable helix (I, II, and IV) folding, unstable helix (III and V) folding, tertiary folding, and finally p53 binding. The folding order for apo-MDM2^N is stable helix (I, II and IV) folding, tertiary folding, and finally unstable helix (III) folding. The difference between the folding pathways of bound MDM2^N and apo-MDM2^N is the reverse of unstable helix folding and tertiary folding, indicating that the unstable helix is stabilized by p53 binding in bound MDM2^N. Note that the extra stability of helix III is offered by unspecific (nonnative) p53 binding contacts because specific (native) binding contacts only occur after tertiary folding.

Entropy Effect in the Binding/Folding Coupling. In the folded state, bound MDM2^N is less heterogeneous than apo-MDM2^N, indicating that the entropy decreases in the presence of p53. This results from specific binding interactions between MDM2^N and p53. The strong and specific binding interactions make the specific binding favorable thermodynamically. In the unfolded state, however, there is no specific binding interaction between the two molecules. Nevertheless, bound MDM2^N is more heterogeneous than that of apo-MDM2^N, so that the entropy increases in the presence of p53. Thus the nonspecific binding of the two molecules is also favorable thermodynamically. Figure 17 presents the thermodynamic circle of entropy changes between bound MDM2^N and apo-MDM2^N and between the folded and unfolded states. Apparently, the entropic effect is highly unfavorable in the coupled folding and binding in the MDM2^N−p53 complex. This unfavorable entropy effect partly weakens the contribution of hydrophobic interactions between p53 and MDM2^N. Therefore bound MDM2^N is only moderately

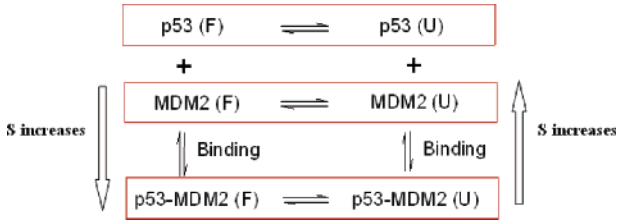

Figure 17. Entropy effect in the folding/binding coupling between p53 and MDM2^N.

more stable upon p53 binding as observed in both experiment and simulation.[9]

Conclusion

We have performed explicit-solvent molecular dynamics simulations (MD) for both bound MDM2^N and apo-MDM2^N to study the interdependence of binding and folding in the p53−MDM2^N complex. Our folded state simulation shows that the MDM2^N binding cleft has to expand upon p53 binding through a rearrangement of the surrounding helices, consistent with the experimental observation.[9] Our folded state simulation further shows that bound MDM2^N is more rigid and less disordered, also in agreement with experimental structural comparison.[9] Kinetics analysis of high-temperature MD simulations shows that both bound MDM2^N and apo-MDM2^N unfold via a two-state process with very similar unfolding rates. Combining unfolding kinetics analysis with transition state analysis for bound MDM2^N and apo-MDM2^N leads to the conclusion that bound MDM2^N is more stable than apo-MDM2^N, in agreement with the previous experimental observation on the relative stabilities between bound MDM2^N and apo-MDM2^N.[9] The entropic effect in the coupled folding and binding in the MDM2^N−p53 complex is found to be highly unfavorable. The unfavorable entropy effect partly weakens the contribution of hydrophobic interactions between p53 and MDM2^N upon the complex stability, resulting in only moderately more stable bound MDM2^N as observed in both experiment and simulation.[9]

Both kinetics and free energy landscape analyses indicate that bound MDM2^N unfolds in the order of p53 unbinding, tertiary unfolding, and finally secondary structure unfolding. Our data show that the unfolding pathways are different between bound MDM2^N and apo-MDM2^N: the unfolding order of unstable helices and tertiary contacts is reversed.

Transition state analysis shows that the transition state of bound MDM2^N is more nativelike and more heterogeneous than that of apo-MDM2^N. Finally we have predicted the Φ-values in both bound MDM2^N and apo-MDM2^N. This experimentally testable prediction suggests that the stable helices (I, II, and IV) are more nativelike than other regions. Within the stable helices, helix II in bound MDM2^N is more nativelike than that in apo-MDM2^N. However, helix I and IV in bound MDM2^N are less nativelike than those in apo-MDM2^N.

Materials and Methods

Room-Temperature and High-Temperature Molecular Dynamics Simulations. The atomic coordinates of the MDM2^N−p53 complex were obtained from the X-ray structure 1YCR.[3] Hydrogen atoms were added using the LEAP module of AMBER8.[35] Counterions were used to maintain system neutrality. All systems were solvated in a truncated

(35) Case, D. A., et al. University of California, San Francisco, 2004.

octahedron box of TIP3P[36] waters with a buffer of 10 Å. Particle Mesh Ewald (PME)[37] was employed to treat long-range electrostatic interactions with the default setting in AMBER8.[35] A revised parm99 force field was used for intramolecular interactions.[38,39] The SHAKE algorithm[40] was used to constrain bonds involving hydrogen atoms. 1000-step steepest descent minimization was performed to relieve any structural clash in the solvated systems. This was followed by heating and brief equilibration for 20 ps in the NVT ensemble at 298 K with SANDER of AMBER8. Langevin dynamics with a time step of 2 fs was used in the heating and equilibration runs with a friction constant of 1 ps^{-1}.

To study the folded state of each solvated system, 10 independent trajectories of 10.0 ns each in the NPT ensemble[41] at 298 K were then simulated with PMEMD of AMBER8. Here molecular dynamics with a time step of 2 fs was used for all production dynamics runs. To study unfolding pathways of each solvated system, 10 independent unfolding trajectories of 10 ns each were performed in the NVT ensemble at 498 K but with the water density at 298 K (i.e., all high-temperature simulations were started from the end of the 10 ns 298 K trajectories). A total of 600 ns trajectories were collected for three solvated systems (bound $MDM2^N$, apo-$MDM2^N$, and p53) at both 298 and 498 K, respectively, taking about 26 400 CPU hours on the in-house Xeon (3.0GHz) cluster.

Native contacts for the bound $MDM2^N$ and apo-$MDM2^N$ were monitored to detect the beginning of unfolded state simulations. It was found that 6 ns at 498 K were needed to reach the equilibrium stage for both bound $MDM2^N$ and apo-$MDM2^N$, so that the first 6 ns (a total of 60 ns for each system) were used to study unfolding kinetics and the remaining 4 ns (a total of 40ns for each system) were used for equilibrium simulations at the unfolded state for each system. The p53 peptide is far less stable; it was found that only 2 ns at 498 K was enough to reach the unfolded state, so that the first 2 ns (a total of 20 ns) were used to study unfolding kinetics, and the remaining 8 ns (a total of 80 ns) were used to study the unfolded equilibrium state.

Transition State Simulations. According to the definition of transition state (TS), 40 test MD runs for each candidate snapshot were performed to calculate the transition probability (P).[30−32] All test simulations have the same initial conformation for protein and solvent atoms but differing initial velocities. Because transition state structures agree with experiment under varying simulation temperatures,[28] TS simulations were done at 498 K in order to accelerate the simulated folding/unfolding rate. Each test trajectory is terminated when a conformation has reached the folded or unfolded state, as determined by Cα-rmsd. The folded state defines as the Cα-rmsd within 3.0 Å from the average structure at the folded state at 298 K. Up to 1 ns simulation at 498 K was found to be sufficient for each test trajectory; i.e., P values for tested snapshots were no longer changing when longer trajectories were run.

Data Analysis. Tertiary contact assignment was handled with in-house software. Two nonadjacent residues are in contact when their Cα atoms are closer than 6.5 Å. Secondary structure assignment was performed with DSSP.[42] All rmsd calculations were performed with PTRAJ in AMBER8.[35] The unfolding kinetics was fitted in Origin 6.1. The unfolding landscapes were determined by calculating normalized probability from a histogram analysis.[30] Here we used the fraction of native tertiary contacts Qf, the fraction of native binding contacts Qb, and the fraction of native helical content H to map the unfolding landscape. Representative structures at folding half times were used to construct unfolding pathways. Each representative structure is the closest snapshot to the average of all chosen snapshots at a given half time (within ± its standard deviation).

Φ-Values were computed with a strategy similar to those used in other studies:[31,43,44]

$$\Phi_i^{\mathrm{calcd}} = \frac{N_i^{\mathrm{TS}} - N_i^{\mathrm{U}}}{N_i^{\mathrm{F}} - N_i^{\mathrm{U}}}$$

where N_i^{TS} is the number of native contacts of residue i at the transition state, and N_i^{F} and N_i^{U} are the number of native contacts of residue i at folded and unfolded states, respectively. As defined by Calfisch and co-workers, contacts were counted when the side chain heavy atoms of two nonadjacent residues are closer than 6 Å.[31] This method has been validated in previous comparative studies of different proteins and found to yield Φ-values in good agreement with experiment.[31,43,44]

Acknowledgment. This work is supported in part by the NIH (GM069620).

Supporting Information Available: Complete ref 35. This material is available free of charge via the Internet at http://pubs.acs.org.

JA0678774

(36) Jorgensen, W. L.; Chandrasekhar, J.; Madura, J. D.; Impey, R. W.; Klein, M. L. *J. Chem. Phys.* **1983**, *79*, 926−935.
(37) Darden, T.; York, D.; Pedersen, L. *J. Chem. Phys.* **1993**, *98*, 10089−10092.
(38) Wang, J. M.; Cieplak, P.; Kollman, P. A. *J. Comput. Chem.* **2000**, *21*, 1049−1074.
(39) Lwin, T. Z.; Lu, Q.; Luo, R. *Protein Sci.* **2006**, *15*, 2642−2655.
(40) Rychaert, J. P.; Ciccotti, G.; and Berendsen, H. J. C. *Comput. Phys.* **1977**, *23*, 327−341.
(41) Berendsen, H. J. C.; Postma, J. P. M.; van Gunsteren, W. F.; DiNola, A.; Haak, J. R. *J. Chem. Phys.* **1984**, *81*, 3684−3690.
(42) Kabsch, W. S. C. *Biopolymers* **1983**, *22*, 2577−2637.
(43) Li, A.; Daggett, V. *Proc. Natl. Acad. Sci. U.S.A.* **1994**, *91*, 10430−10434.
(44) Vendruscolo, M.; Paci, E.; Dobson, C. M.; Karplus, M. *Nature* **2001**, *409*, 641−645.